AIAA 2012-4962
Local Orbital Debris Flux Study in the Geostationary Ring

Paul V. Anderson and Hanspeter Schaub

University of Colorado, Boulder, CO, 80309, USA

AIAA Astrodynamics Specialist Conference
August 13–16, 2012 / Minneapolis, MN

Local Orbital Debris Flux Study in the Geostationary Ring

Paul V. Anderson* and Hanspeter Schaub†
University of Colorado, Boulder, CO, 80309, USA

A local orbit debris flux study is performed in the geostationary (GEO) ring to investigate how often near-miss events occur for each longitude slot at this GEO altitude. The current resident space object (RSO) environment near GEO is evaluated, and publicly-available two-line element (TLE) data are utilized in tandem with a geostationary torus configuration to simulate near-miss events incurred by the trackable RSO population at GEO. Methodology for determining near-miss events with this formulation is introduced, and the results of the study for a one-year period are presented to illustrate the importance of GEO remediation.

I Introduction

THE geostationary (GEO) ring is a precious commodity of the terrestrial satellite industry that has become contaminated with an alarming number of orbital debris objects.[1,2,3,4] Defunct, decommissioned satellites, upper launch vehicle stages, and fragmentation particulates continuously threaten spacecraft operating within this regime. As a lack of atmospheric drag effects at the GEO altitude renders the lifetimes of these debris objects infinitely long,[5,6,7,8] conjunction and mitigation assessment must be performed to safeguard functional GEO satellites from colliding with the surrounding debris field. GEO satellites must maintain a specific longitude, and therefore cannot simply phase shift to evade debris – analysis of the *macroscopic* behavior of the geosynchronous debris field is therefore required to describe debris fluxes through GEO longitude slots, to forecast how often operational satellites in these regions must potentially perform maneuvers to mitigate conjunction scenarios. Instead of presenting highly-accurate analysis required for risk assessment and mitigation,[9,10] this study fills a void in the literature by illustrating gross behavior of the resident space object (RSO) population at GEO, to discern which *local* regions of the GEO ring are most susceptible to rising debris fluxes at different times.

Existing debris analysis and evolution software[11,12,13] use inertial cell definitions to track debris cell passage events (CPE) arising from the intersections of osculating RSO orbits with the cells of interest during long-term propagation. Using various probability models, the associated spatial density and flux contributions for each CPE may thereafter be computed and implemented in collision risk assessment. For the GEO regime, these analysis tools often average in cell right ascension, providing debris fluxes as a function of altitude and declination.[7] Furthermore, employing inertially-fixed cell definitions only, flux contributions to particular GEO longitude slots at arbitrary times cannot be determined. Therefore, though *average* flux conditions at GEO may be estimated with such tools, *local* intersection events for certain longitude slots are not accessible – the latter is of interest to space operators concerned with the debris conditions near a functioning satellite. This study implements a toroidal cell configuration at the GEO altitude to evaluate the impact of the current RSO population on the longitude slots at GEO, by performing a *near-miss analysis* that attempts to quantify the frequency at which uncontrolled RSOs pass within a given distance of a particular slot. Thus, to enhance intuition, an integer number of near-misses is used here as the alternative to typical[7] density and flux metrics.

Such a near-miss analysis is critical, as it establishes a metric as to how often a GEO satellite operator will have to track nearby debris motion, and execute avoidance maneuvers. The latter is of particular importance, as GEO satellites are flying at this altitude to avoid extensive station-keeping fuel expenditures. Therefore, as the RSO population near GEO continues to increase, the amount of fuel required to remain at a longitude slot while avoiding debris will increase as well. The focus of this analysis is to propose a near-miss metric and illustrate current conditions at GEO. The metric

*Graduate Student, Department of Aerospace Engineering Sciences, 429 UCB, Boulder, CO, 80309. AIAA Student Member.
†Associate Professor, Associate Chair of Graduate Affairs, Department of Aerospace Engineering Sciences, 429 UCB, Boulder, CO, 80309. AIAA Associate Member.

can then be used in future work as the impact of continued, uninhibited debris generation – or conversely, active GEO RSO removal to disposal orbits – is investigated.

Although current probability of collision at GEO has been assessed as relatively low as compared to that within the low-Earth orbit (LEO) regime,[4,14] collision risk will increase if mitigation and remediation measures are not globally adopted and implemented. This study illustrates the current status of near-miss events at GEO, given the present, and trackable, RSO population in this ring, to serve as a benchmark for continuing studies that will demonstrate the future severity of this environment under projected growth without remediation. Total insurance value of on-orbit assets in the GEO regime is estimated at USD 20 billion[4] – debris analysis studies therefore have strong implications for satellite owners/operators that desire to preserve the continued usefulness of this resource, by forecasting debris field evolution and providing recommendations for mitigation at GEO.

II Current RSO Population at GEO

The status of the RSO population currently in the geostationary regime is presented as a precursor to the flux study performed. Section II.A describes the RSO classification system implemented and highlights the tracking data source utilized; Section II.B briefly illustrates the distribution of this RSO population.

II.A Classification of Geosynchronous Objects

The RSO population in the geostationary regime is classified with a taxonomy implemented by the European Space Agency's DISCOS Database (Database and Information System Characterising Objects in Space) and updated by the European Space Operations Centre's (ESOC) Space Debris Office.[15] For geosynchronous RSOs, seven orbit categories are established to classify the type of geosynchronous orbits traversed by these objects; Table 1 provides a description of this classification system. Geostationary objects are selected according to[15]

- Eccentricity smaller than 0.2 ($e < 0.2$);
- Inclination smaller than 70° ($i < 70^\circ$);
- Mean motion between 0.9 and 1.1 revolutions per sidereal day ($0.9 < n < 1.1$).

Orbital data for the trackable GEO RSO population are obtained from publicly-available two-line element (TLE) sets provided by the U.S. Strategic Command (USSTRATCOM).[a] For this debris flux study, a reference TLE set obtained on 15 February 2012 is implemented; the class distribution for the 1070 objects extracted from this set is illustrated in Figure 1. Note that while approximately one-third of this RSO population is under control, *half* of this population is hazardously drifting above, below, or through the GEO altitude. Figure 2 quantifies the influence of eccentricity on the penetration of the GEO protection zone, defined as a 200-km torus bounding the GEO ring.[16,17] Though the semi-major axis of a given RSO may deviate from the geostationary radius, high eccentricity may "slingshot" such an object through this protection zone towards radius of perigee or apogee.

TLE data are provided as mean Keplerian elements[7] with mean motion instead of semi-major axis, converted into osculating elements with Brouwer-Lyddane theory[18] for this flux study. The TLE data provide additional information on the reference TLE epoch and international designation code (COSPAR[b] designation) for each of the tracked objects. Note that because of the limited accuracy of these TLE sets, TLE data are *not meant for high-precision analyses*; as the purpose of this study is to characterize near-miss events occurring on a macroscopic scale, the accuracy of these data is appropriate for this study. Furthermore, only objects larger than 1-m are routinely tracked[c] at this GEO altitude;[15] thus, only RSOs at least of this size are considered.

Additionally, note that although 1070 objects from the 15 February 2012 USSTRATCOM TLE satisfied the criteria provided above for a GEO designation, 238 more objects without up-to-date TLE data are known to reside within this regime[15] – therefore, there exist a total of 1308 known RSOs near the geosynchronous altitude. In Reference 15, orbit data for 164 of the 238 objects for which current tracking data are not available were provided by the Keldysh Institute for Applied Mathematics (KIAM); these RSOs are not accounted for here.

[a] Publicly-available TLE sets (updated twice daily) are available for bulk download from: `https://www.space-track.org/`

[b] During processing of a TLE data set, COSPAR identifiers are checked against Reference 15 (COGO-14) for class assignment.

[c] USSTRATCOM collects tracking data for GEO with the GEODSS (Ground-Based Electro-Optical Deep-Space Surveillance) and MOTIF (Maui Optical Tracking and Identification Facility) installations, part of the Space Surveillance Network (SSN).[7]

Table 1: Orbit classifications of geosynchronous objects employed for GEO debris flux study.

Class	Type	Description
C1	Controlled	Under longitude and inclination control (E-W and N-S control)
C2	Controlled	Under longitude control only (E-W control)
D	Drifting	Drifting above, below, or through GEO ring
L1	Librating	Libration orbit about the Eastern stable point ($\lambda = 75°$E)
L2	Librating	Libration orbit about the Western stable point ($\lambda = 105°$W)
L3	Librating	Libration orbit about both stable points
IN	Indeterminate	Unknown status (e.g., recent TLE not available)

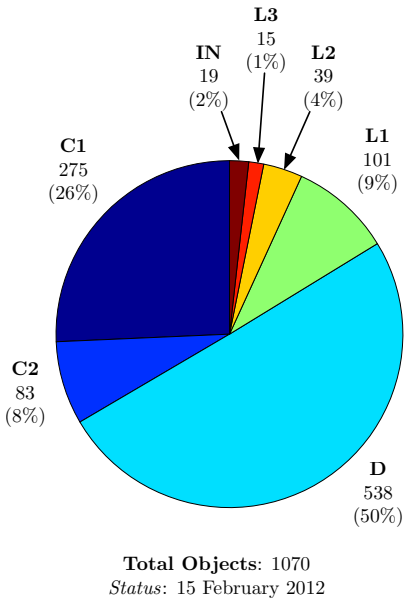

Figure 1: Classification of GEO RSO population.

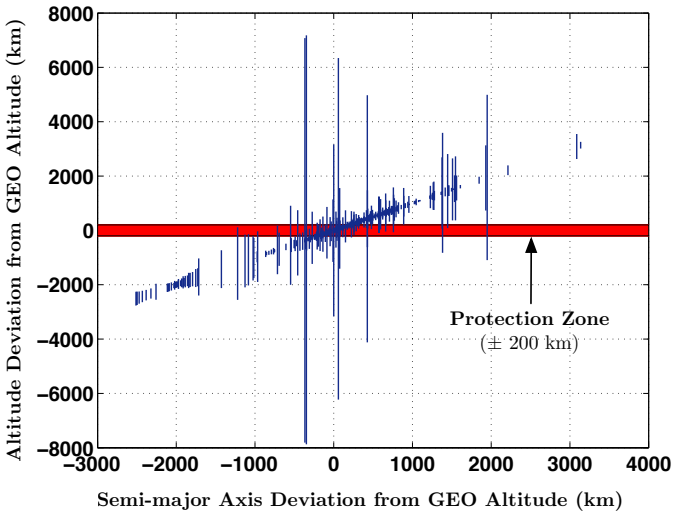

Figure 2: Distribution of drifting population (each line represents one RSO). GEO protection zone requirements obtained from NASA[16] and ESA.[17]

II.B Distribution of Geosynchronous Objects

Using the 15 February 2012 reference TLE considered for this study, the projected RSO population distribution as of 01 March 2012 (the start date for the near-miss CPE analysis) is evaluated using the orbital propagator detailed in Section III.C. Visualization of the geostationary RSO population on this date (epoch 00:00:000 UTCG) is provided in Figure 3(a); the longitude distribution of these 1070 RSOs is illustrated in Figure 3(b). Note the high concentration of librating RSOs (*red*) in the vicinity of the Eastern and Western stable points. Drifting objects (*cyan*), though distributed approximately uniformly around the GEO regime, pose less of a hazard to the longitude slots over the Pacific Ocean, in which controlled C1/C2 on-orbit assets are at a minimum. Thus, instead of stipulating *average* spatial RSO density in the GEO ring, this study seeks to evaluate *localized* densities by simulating near-miss events for each longitude slot.

III Local Debris Flux Study at GEO

A debris flux analysis in the GEO ring is performed to quantify the number of near-misses occurring in a particular time frame for every longitude slot at GEO – thereby, the results of this study seek to quantify *how often* operational satellites residing within this regime potentially need to maneuver to avoid impending conjunction with a nearby RSO, given the current trackable debris population in the geosynchronous regime. Section III.A presents the torus concept employed for performing this study, and Section III.B mathematically formulates near-miss intersections. Section III.C describes the force model implemented in propagation, and Section III.D presents the results of the study for a one-year period to forecast current "debris weather" at GEO.

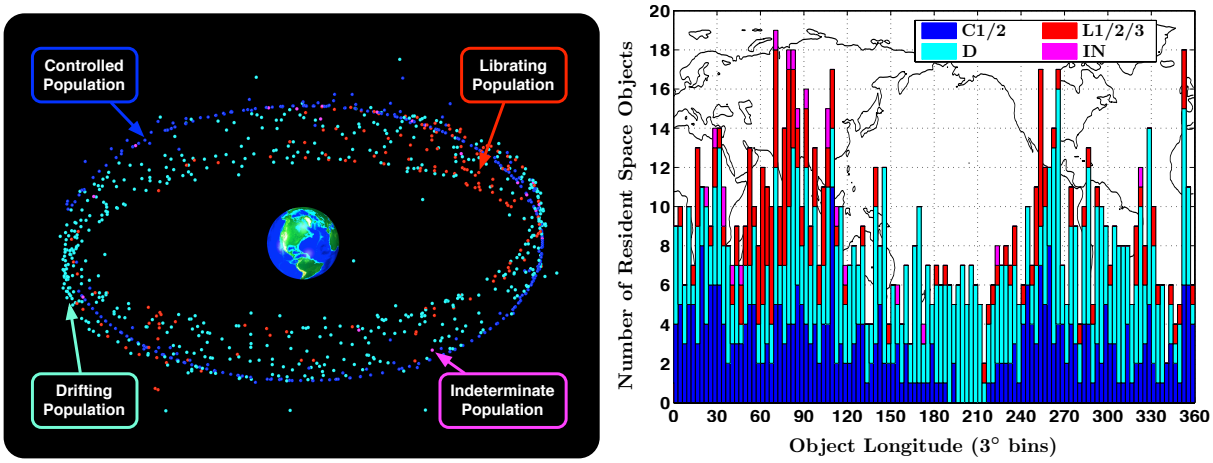

a) Visualization of RSO population at GEO.

b) Longitude distribution of RSO population at GEO.

Figure 3: Projected distribution of GEO RSO population on 01 March 2012 using 15 February 2012 TLE set.

III.A Geostationary Torus Concept

Near-miss events for GEO longitude slots are quantified by formulating a GEO-encompassing torus of major radius 42164 km and minor radius $\tilde{r}$, as shown in Figure 4. Torus cells used for tracking the near-miss CPE are constructed by partitioning this torus with longitude increments of $\Delta\lambda$. For this analysis, $\Delta\lambda = 1^\circ$ is utilized, and minor radii of $\tilde{r} = 50 \text{ km}, 100 \text{ km}, 300 \text{ km}, 700 \text{ km}$ are simulated to evaluate the frequency of near-miss CPE occurring from distances representative of a one degree longitude slot at GEO ($\sim$700 km) to distances at which precise conjunction assessment and analysis are considered ($\sim$50 km). Furthermore, this torus formulation is a natural choice for evaluating CPE for the non-inertial GEO longitude slots – the torus geometry is invariant as seen by both the inertial J2000 frame and the Earth-centered, Earth-fixed frame (in which these longitude slots are fixed). Thus, coordinate transformations are not required in this formulation.

Furthermore, Figure 4 also illustrates several examples of complex relative RSO motion experienced by operational GEO satellites in the course of one day. As natural perturbations (especially the lunar gravity influence) increase the inclination of near-synchronous RSOs, but do not appreciably alter the orbital radius, these objects trace north-south routes that interact with the GEO ring at ascending and descending nodes.[5] Geosynchronous, inclined RSOs exhibit a north-south motion that appears as a straight line from an observer fixed to the Earth. The near-synchronous objects that deviate from the GEO altitude additionally exhibit an eastward/westward drift that superimposes upon this north-south motion to establish the sinusoidal and "figure-8" trajectories illustrated in Figure 4 – these relative orbits precess eastward for RSOs below the GEO altitude, and regress westward for RSOs above the GEO altitude. In each of these cases, luni-solar gravitation induces an increase in orbit inclination of approximately 0.8° per year.[5]

III.B Formulation of Cell Passage Events

III.B.1 Mathematical Specification

Near-miss CPE are detected during forward propagation of a particular near-synchronous RSO by checking for transversal of the GEO torus boundary at each time step of numerical integration (the integration routine used for this research is highlighted below within Section III.C). Mathematically, a near-miss event occurs if

$$\left(r_{\text{GEO}} - \sqrt{r_X^2 + r_Y^2}\right)^2 + r_Z^2 - \tilde{r} < 0 \tag{1}$$

is satisfied, wherein $(r_X, r_Y, r_Z)^T$ is the RSO position vector expressed in the inertial J2000 reference frame, $r_{\text{GEO}} = 42164$ km is the major torus radius, and $\tilde{r}$ is the specified minor radius. The longitude of intersection λ_{CPE} is thereafter determined with

$$\lambda_{\text{CPE}} = \arctan\left(\frac{r_Y}{r_X}\right) - \alpha_G \tag{2}$$

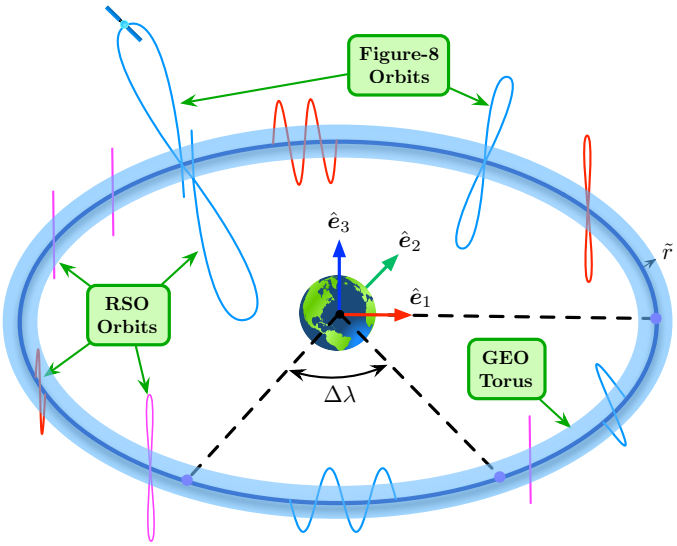

Figure 4: Geostationary torus concept implemented in near-miss study.

wherein α_G is the right ascension of Greenwich, determined with the following methodology:[19]

$$J_0 = 367t_y - \text{floor}\left(\frac{7}{4}\left[t_y + \text{floor}\left(\frac{t_m + 9}{12}\right)\right]\right) + \text{floor}\left(\frac{275t_m}{9}\right) + t_d + 1721013.5 \tag{3a}$$

$$T_0 = \frac{J_0 - 2451545}{36525} \tag{3b}$$

$$\alpha_{G0} = 100.4606184 + 36000.77004\,T_0 + 0.000387933\,T_0^2 - 2.583\left(10^{-8}\right)T_0^3 \tag{3c}$$

$$\alpha_G = \alpha_{G0} + 360.98564724\left(\frac{t_h}{24}\right) \tag{3d}$$

In this formulation, the current propagation time is expressed with (t_y, t_m, t_d, t_h), corresponding to the year, month, day, and hour (e.g., universal time) of the current simulation epoch.[d] Thus, when a torus-intersection is detected with Equation (1), the instantaneous longitude of intersection is determined with Equation (2), and the total CPE count for the appropriate torus cell is updated. Again, note that because of the convenient invariance of this torus geometry, the inertial RSO coordinates obtained during the numerical integration do not need to be converted into the rotating Earth-centered, Earth-fixed reference frame to check for intersections. This elegant property provides for significant computational speedups that enable shorter simulation runtimes.

To ensure that similar intersection events are not accounted for more than once during this CPE checking, counting logic is employed *before* a cell intersection counter is updated to "screen" the event for redundancy. Figure 5 illustrates several examples as to how near-miss intersection events are counted during simulations. Relative orbits that reside entirely inside a particular torus cell, as illustrated within Figure 5(a), are counted only once during the specified CPE tracking interval[e]; if the RSO exits and subsequently re-enters this torus cell, however, additional near-miss events are accounted for following each re-entry, as shown in Figures 5(b)-5(c). Furthermore, additional near-miss events are counted if the relative orbit drifts into a neighboring cell during the CPE tracking interval of interest; Figures 5(d)-5(e) illustrate situations in which one and two near-misses are recorded per cell, respectively. This counting methodology ensures that near-miss events are tracked for each of the longitude slots in a logical, consistent, and non-redundant manner for the entirety of the interval. After propagating through the full interval, all cell counts are output and zeroed, and propagation continues. The complete algorithm for determining near-miss events with the torus scheme is detailed in Section III.B.2.

[d]For concise explanation as to the Julian date and time parameters used in this method, the reader is referred to Reference 19.

[e]Arbitrary CPE tracking intervals are defined to catalog intersections in consistent, reoccurring time frames. For this study, near-miss events are tracked in one-day intervals – after every day of propagation, torus cell counts are output and then zeroed.

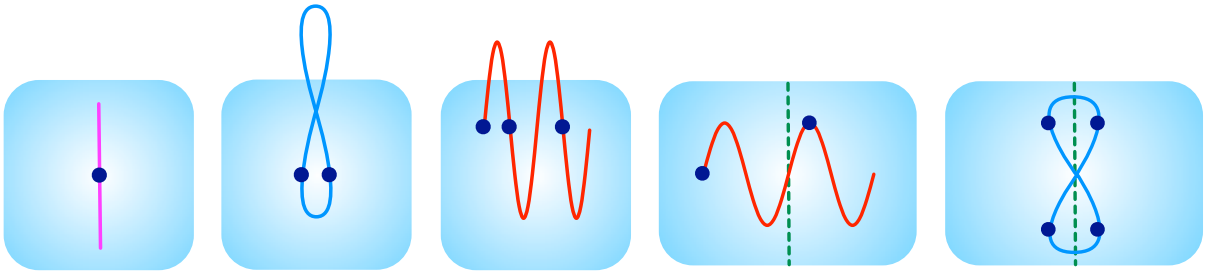

a) Count: 1 **b)** Count: 2 **c)** Count: 3 **d)** Count: 1 per cell **e)** Count: 2 per cell

Figure 5: Examples of counting logic implemented to eliminate redundancy in CPE intersection checking.

III.B.2 CPE Algorithm for Torus Formulation

Let t_i denote the epoch of the i^{th} RSO, and let t, t_{int}, and t_f denote the integration time, CPE interval time, and final simulation time, respectively. Define N_{RSO} as the number of geosynchronous RSOs, and $N_{\text{CPE}}|_{\lambda_{\text{bin}}}$ as the number of near-miss events for the torus cell indexed by longitude bin λ_{bin}. Furthermore, let $\mathcal{C}$ denote the set of all C1/C2 objects, and let $\mathcal{D}$, $\mathcal{L}$, and $\mathcal{I}$ be the sets of all D, L1/L2/L3, and IN objects, respectively. The algorithm for evaluating near-miss events with the GEO torus formulation is provided as follows:

while $t_i < t_f$ **do**
  for $i = 1 \rightarrow N_{\text{RSO}}$ **do**
    Intersection flag $\leftarrow 0$
    Longitude flag $\leftarrow -1$
    if $i \in \mathcal{D} \cup \mathcal{L} \cup \mathcal{I}$ **then**
      while $t < t_{\text{int}}$ **do**
        Propagate: $t \leftarrow t + \Delta t \Rightarrow \boldsymbol{r}_{\text{RSO}} = (r_X, r_Y, r_Z)^T$
        if $(r_{\text{GEO}} - \sqrt{r_X^2 + r_Y^2})^2 + r_Z^2 - \tilde{r} < 0$ **then**
          $t_h \leftarrow t_i + t/3600$
          Compute $\alpha_G \Leftarrow$ Equations (3a)-(3d)
          $\lambda_{\text{CPE}} = \texttt{atan2}(r_Y, r_X) - \alpha_G$
          $\lambda_{\text{bin}} = \text{floor}(\lambda_{\text{CPE}})$
          if Intersection flag = 0 $\|$ Longitude flag $\neq \lambda_{\text{bin}}$ **then**
            Increment: $N_{\text{CPE}}|_{\lambda_{\text{bin}}} \leftarrow N_{\text{CPE}}|_{\lambda_{\text{bin}}} + 1$
            Longitude flag $\leftarrow \lambda_{\text{bin}}$
          end if
        end if
        if $(r_{\text{GEO}} - \sqrt{r_X^2 + r_Y^2})^2 + r_Z^2 - \tilde{r} < 0$ **then**
          Intersection flag $\leftarrow 1$
        else
          Intersection flag $\leftarrow 0$
        end if
      end while
      $t_i \leftarrow t_i + t_{\text{int}}$
      Update RSO fields
    else $(i \in \mathcal{C})$
      $t_i \leftarrow t_i + t_{\text{int}}$
      Update $\boldsymbol{r}_{\text{RSO}} \leftarrow \lambda_i$ maintained
      Update RSO fields
    end if
  end for
  Output $N_{\text{CPE}}|_{\lambda_{\text{bin}}} \; \forall \; \lambda_{\text{bin}} \in [0^\circ, 360^\circ)$
  $N_{\text{CPE}}|_{\lambda_{\text{bin}}} = 0 \; \forall \; \lambda_{\text{bin}} \in [0^\circ, 360^\circ)$
end while

III.C Propagator and Implementation

During propagation of the GEO RSO population, variable-step Runge-Kutta methodology is utilized to numerically integrate the equations of motion under a force model representative of the geostationary ring. Thus, an 8×8 spherical harmonics expansion of the Earth's gravitational field is implemented with third-body luni-solar perturbations and a nominal solar radiation pressure (SRP) disturbance. Specifically,

$$\ddot{\boldsymbol{r}} = -\frac{\mu_\oplus}{r^3}\boldsymbol{r} + \boldsymbol{a}_\oplus + \boldsymbol{a}_\leftmoon + \boldsymbol{a}_\odot + \boldsymbol{a}_{\text{SRP}} \tag{4}$$

where the first term denotes Keplerian two-body acceleration, $\boldsymbol{a}_\oplus$ is the acceleration due to the nonsphericity of Earth, $\boldsymbol{a}_\leftmoon$ and $\boldsymbol{a}_\odot$ denote the third-body contributions from the Moon and Sun, respectively, and $\boldsymbol{a}_{\text{SRP}}$ is the solar radiation pressure acceleration. In the noninertial Earth-centered, Earth-fixed (ECEF) frame, $\boldsymbol{a}_\oplus$ is written[20]

$$a_\oplus^x = \left(\frac{1}{r}\frac{\partial U}{\partial r} - \frac{r_z}{r^2\sqrt{r_x^2+r_y^2}}\frac{\partial U}{\partial \phi}\right) r_x - \left(\frac{1}{r_x^2+r_y^2}\frac{\partial U}{\partial \lambda}\right) r_y \tag{5}$$

$$a_\oplus^y = \left(\frac{1}{r}\frac{\partial U}{\partial r} - \frac{r_z}{r^2\sqrt{r_x^2+r_y^2}}\frac{\partial U}{\partial \phi}\right) r_y + \left(\frac{1}{r_x^2+r_y^2}\frac{\partial U}{\partial \lambda}\right) r_x \tag{6}$$

$$a_\oplus^z = \frac{r_z}{r}\frac{\partial U}{\partial r} + \frac{\sqrt{r_x^2+r_y^2}}{r^2}\frac{\partial U}{\partial \phi} \tag{7}$$

where $\boldsymbol{r} \equiv (r_x, r_y, r_z)^T$ is the RSO position vector expressed within the Earth-centered, Earth-fixed reference frame, ϕ and λ denote geocentric latitude and longitude, respectively, and the partial derivatives are written[20]

$$\frac{\partial U}{\partial r} = -\frac{\mu_\oplus}{r^2}\sum_{l=2}^{\infty}\sum_{m=0}^{l}\left(\frac{R_\oplus}{r}\right)^l (l+1)P_{l,m}(\sin\phi)\Big[C_{l,m}\cos(m\lambda) + S_{l,m}\sin(m\lambda)\Big] \tag{8}$$

$$\begin{aligned}\frac{\partial U}{\partial \phi} = \frac{\mu_\oplus}{r}\sum_{l=2}^{\infty}\sum_{m=0}^{l}\left(\frac{R_\oplus}{r}\right)^l &\Big[P_{l,m+1}(\sin\phi) - m\tan(\phi)P_{l,m}(\sin\phi)\Big] \\ &\times \Big[C_{l,m}\cos(m\lambda) + S_{l,m}\sin(m\lambda)\Big]\end{aligned} \tag{9}$$

$$\frac{\partial U}{\partial \lambda} = \frac{\mu_\oplus}{r}\sum_{l=2}^{\infty}\sum_{m=0}^{l}\left(\frac{R_\oplus}{r}\right)^l mP_{l,m}(\sin\phi)\Big[S_{l,m}\cos(m\lambda) - C_{l,m}\sin(m\lambda)\Big] \tag{10}$$

In this formulation, $R_\oplus = 6378.137$ km denotes Earth's equatorial radius, $P_{l,m}$ are the associated Legendre functions of degree l and order m, $C_{l,m}$ and $S_{l,m}$ are the un-normalized Stokes coefficients of the EGM-96 gravity model[f], and

$$\sin\phi = \frac{r_z}{r} \tag{11}$$

$$\tan\lambda = \frac{r_y}{r_x} \tag{12}$$

Note that since Equations (5)-(7) are expressed in the rotating ECEF frame, this acceleration vector $\boldsymbol{a}_\oplus$ is transformed into inertial frame (e.g., J2000) coordinates during integration. The third-body acceleration arising from the direct and indirect effects of luni-solar gravitation are written[20]

$$\boldsymbol{a}_\leftmoon = \mu_\leftmoon\left(\frac{\boldsymbol{r}_{j,\leftmoon}}{r_{j,\leftmoon}^3} - \frac{\boldsymbol{r}_{\oplus,\leftmoon}}{r_{\oplus,\leftmoon}^3}\right) \tag{13}$$

$$\boldsymbol{a}_\odot = \mu_\odot\left(\frac{\boldsymbol{r}_{j,\odot}}{r_{j,\odot}^3} - \frac{\boldsymbol{r}_{\oplus,\odot}}{r_{\oplus,\odot}^3}\right) \tag{14}$$

[f]Normalized Stokes coefficients for the EGM-96 model may be obtained at: `http://cddis.nasa.gov/926/egm96/egm96.html` For details as to un-normalizing the Stokes coefficients for use in the spherical harmonics gravity model, the reader is referred to Reference 20.

where $\boldsymbol{r}_{j,\leftmoon/\odot}$ denotes the inertial position vector from the j^{th} RSO to the Moon and Sun, respectively, and $\boldsymbol{r}_{\oplus,\leftmoon/\odot}$ is the inertial position vector from the Earth to the Moon and Sun, respectively. The constants $\mu_{\leftmoon} \equiv GM_{\leftmoon}$ and $\mu_{\odot} \equiv GM_{\odot}$ denote the gravitational parameters for the Moon and Sun – these third bodies thus *directly* influence RSO orbits, and furthermore exert an *indirect* effect via gravitational interactions with Earth. The solar radiation pressure acceleration $\boldsymbol{a}_{\text{SRP}}$ is modeled with the spherical "cannonball" formulation as follows:[20]

$$\boldsymbol{a}_{\text{SRP}} = -p_{\text{SRP}} c_r \beta \left(\frac{\boldsymbol{r}_{j,\odot}}{r_{j,\odot}} \right) \tag{15}$$

wherein p_{SRP} denotes the solar radiation pressure at the altitude of the RSO orbit[g], $c_r \equiv 1.5$ denotes the coefficient of reflectivity, and $\beta \equiv A_{\odot}/m$ is the area-to-mass ratio of the considered object. Preliminary research[21] indicates that $\beta \approx 0.04$ m^2/kg is representative of the geosynchronous RSO population – therefore, this value is implemented for the "nominal" solar radiation pressure perturbation *for all* RSOs[h] during propagation of the debris field.

The RSO propagation routine is written in ANSI-C and applies a variable-step Runge-Kutta-45 integration method. During initial propagation of the debris field to the desired CPE start date, a 10-minute time step is specified. During near-miss computations in the time frame of interest, this time step is decreased to 1-minute for an augmented fidelity during simultaneous propagation and CPE-checking activities. Note that although this integrator and force model have been verified with NASA's General Mission Analysis Tool (GMAT)[i] for brief integration periods, they *are not intended* to provide a high-precision propagation utility.[j] A flowchart presenting a high-level description of debris processing, propagation, and analysis is illustrated in Figure 6.

III.D Results of Debris Flux Study

The results of the geostationary debris flux analysis performed from March 2012 – March 2013 for each of the four minor radius $\tilde{r}$ configurations considered are illustrated within Figure 7. For this scenario, the GEO debris population was propagated without solar radiation pressure effects, and near-miss CPE were checked every 1-minute of integration with daily CPE intervals (t_{int} = 86400 s). Note that because this flux study only incorporates near-miss events for the trackable, catalogued near-synchronous objects, these findings serve as a *lower bound* for the true flux situation in the GEO regime. As anticipated, as the torus radius $\tilde{r}$ increases, the near-miss CPE become more pronounced throughout the simulation space, exhibiting the severest "debris weather" at the locations of the Eastern ($\lambda = 75^{\circ}$) and Western ($\lambda = 255^{\circ}$) stable points for the entire period. Note that regions of increased near-miss events could be generated with (*a*) multiple RSOs with single events over the daily CPE interval, or (*b*) single RSOs with multiple intersection events over this CPE cycle, or (*c*) a combination of the above, in which complex relative motion induces the spatially-dense regions of Figure 7.

The stochastic signature of the near-miss events illustrated in Figure 7 emerges from a superposition of individual linear and quasi-linear traces generated with near-synchronous RSO orbits that deviate from the GEO altitude – these objects demonstrate a drift magnitude indicated by the slopes of their observed traces. Traces of positive slope indicate eastward precession (*below* GEO), while traces of negative slope conversely denote westward regression (*above* GEO). As all objects exhibiting mean motion $0.9 < n < 1.1$ revs/day are included in this analysis (Section II.A), and noting that the slopes of these traces are given with $(n - n_{\text{GEO}})^{-1}$, the observed slopes have an upper bound of 35°/day for the eastward-drifting RSOs, and -37°/day for the westward-drifting RSOs – objects *exactly* at GEO appear as vertical traces of an ∞ slope. Quasi-linear traces examined within Figure 7 exhibit a curvature that arises from the oscillatory characteristic of the librating RSOs that achieve their amplitude of oscillation and begin regressing, with a period $T_{\text{L}} \approx 1.5$ years at minimum.[22]

Individual orbit class contributions to the $\tilde{r} = 300$ km case shown within Figure 7(c) are illustrated in Figure 8. As D objects constitute half of the trackable RSO population at GEO (Figure 1), this drifting contribution is the most pronounced and visibly stochastic; the near-vertical traces of several RSOs drifting close to the GEO ring are perceptible in Figure 8(a). Regions of increased RSO congestion in the vicinity of the Eastern and Western stable points are driven primarily by near-miss contributions from the L1/L2 librating objects, as illustrated in Figures 8(b)-8(c). Quasi-linear traces exhibited by the majority of IN objects in Figure 8(d) indicate that these particular RSOs may belong to one of the librating (L1/L2/L3) categories. Although the superposition of each of these class contributions yields a result that

[g] Solar radiation pressure is modeled using an inverse-square diffusion formulation of solar luminosity $L_{\odot} \approx 3.839 \times 10^{26}$ J/s.

[h] Instituting individual β_j for each RSO is a nontrivial matter and not in accordance with the purposes of this research.

[i] NASA's GMAT mission design software is open-source and publicly-available from: `http://gmat.gsfc.nasa.gov/`

[j] The purpose of this study is to highlight *macroscopic* patterns and trends in geosynchronous RSO motion - this propagation routine agrees with GMAT to within 3-km RSS after one month of integration, suitable for the goals of this near-miss analysis.

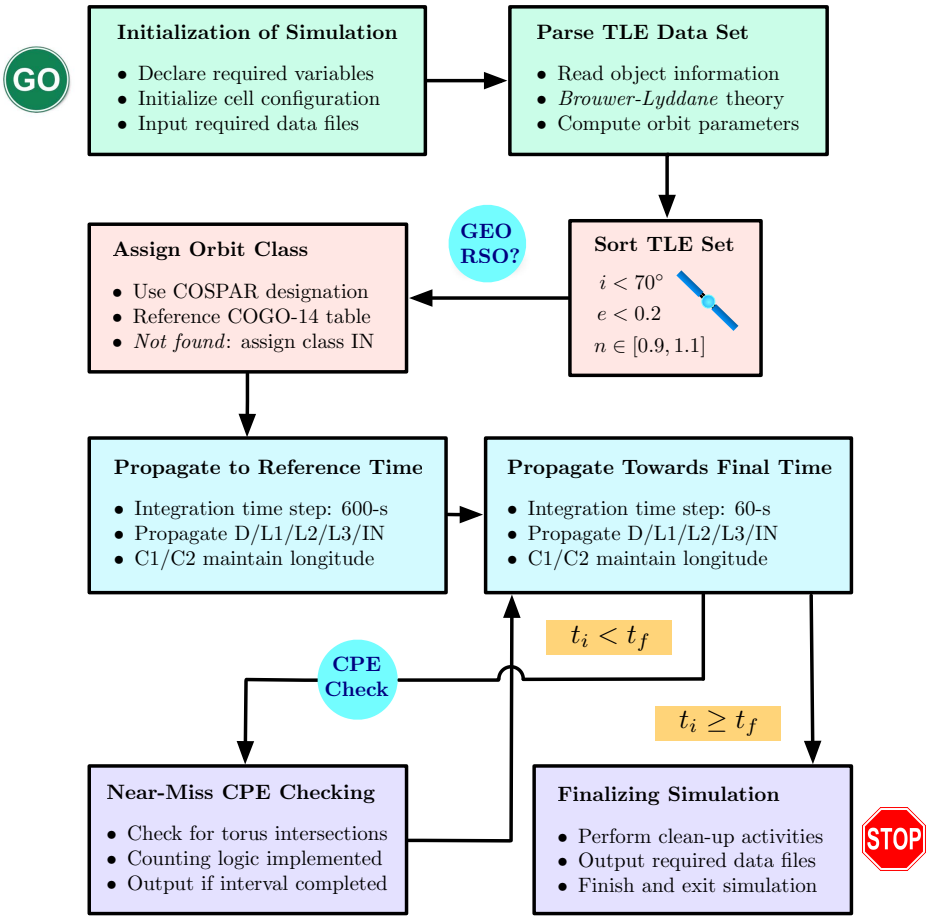

Figure 6: Illustration of high-level workflow for processing, propagation, and analysis of TLE data.

is of a more stochastic than deterministic signature, this flux analysis illustrates that regions of increased spatial density do exist *locally*, centered around the Eastern and Western gravitational wells. This notion has important implications for satellite owners/operators with on-orbit assets in the neighborhoods of these "stormy" locations in the GEO ring.

With nominal solar radiation pressure included within the debris propagation, the results of an equivalent debris flux study performed from March 2012 – March 2013 for each of the four $\tilde{r}$ configurations are shown in Figure 9. As anticipated, Figure 9 illustrates no appreciable deviation from the case without nominal SRP, as illustrated in Figure 7; the area-to-mass ratio $\beta = 0.04$ m^2/kg used for simulating nominal SRP (Section III.C) is not sizable enough to incur substantial differences in the simulation results in this one-year time frame. For lengthier CPE simulation time spans, it is critical to incorporate the long-term influence of SRP, but for the purposes of this research, an equivalent fidelity is achieved with or without this disturbance; the representative β value is low enough to ensure that the inclusion of SRP does not impact simulation findings.

IV Conclusion

An orbital debris flux study is performed in the geostationary regime to investigate the number of near-miss events occurring for each longitude slot at GEO. A geostationary torus configuration is implemented in tandem with publicly-available TLE data to simulate near-miss CPE incurred by the current GEO RSO population during the March 2012 – March 2013 time frame. Though these simulation results indicate that GEO "debris weather" is primarily stochastic in nature, these findings demonstrate that two regions of increased RSO congestion do exist at GEO, centered around the Eastern and Western stable points within the gravitational field. Though the frequency of near-miss events occurring at the GEO altitude is still relatively low as compared to LEO, appropriate remediation measures need to be implemented *now*, to protect future usefulness of this resource and driver for space development, and preclude a situation similar to that now present in LEO.

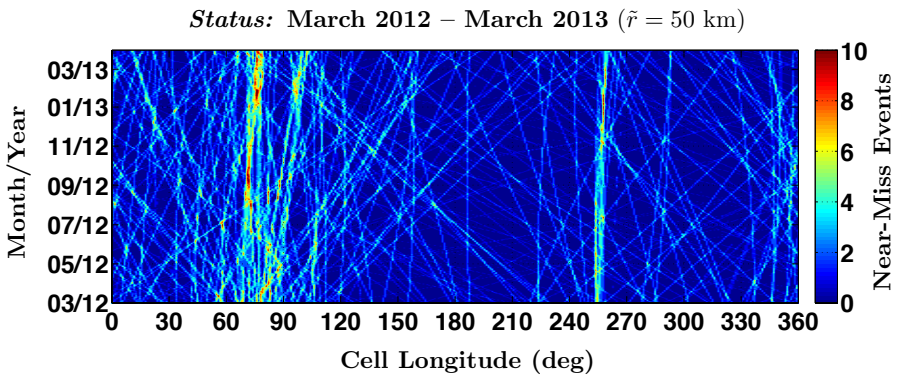

a) Near-miss CPE for March 2012 – March 2013 for 50-km GEO torus.

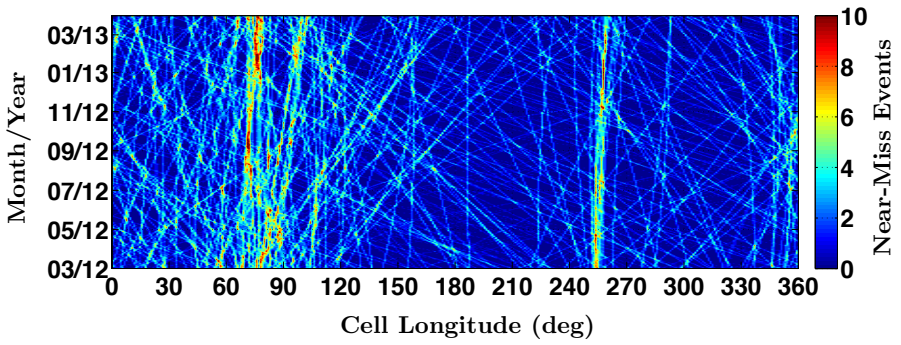

b) Near-miss CPE for March 2012 – March 2013 for 100-km GEO torus.

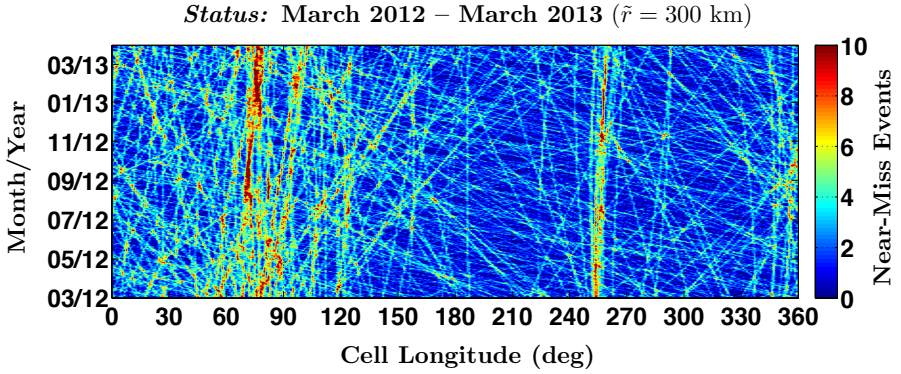

c) Near-miss CPE for March 2012 – March 2013 for 300-km GEO torus.

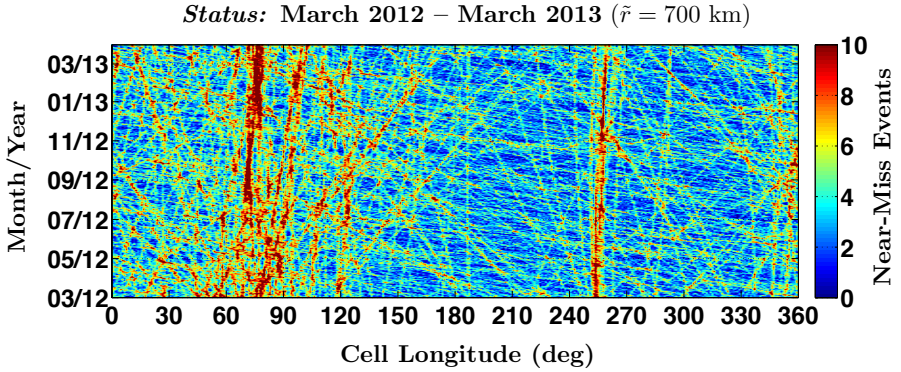

d) Near-miss CPE for March 2012 – March 2013 for 700-km GEO torus.

Figure 7: Near-miss CPE for March 2012 – March 2013 without SRP.

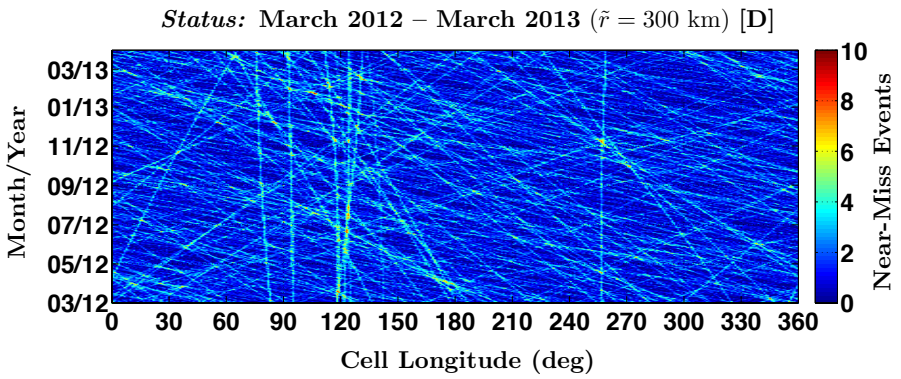

a) Drifting object (D) contribution to near-miss CPE simulation.

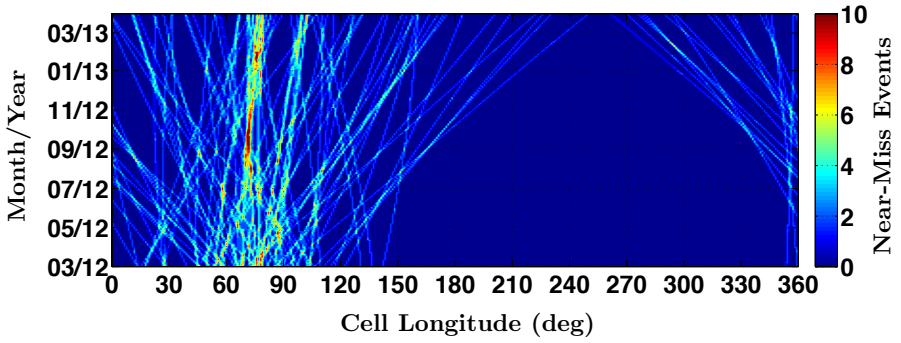

b) Eastern librating object (L1) contribution to near-miss CPE simulation.

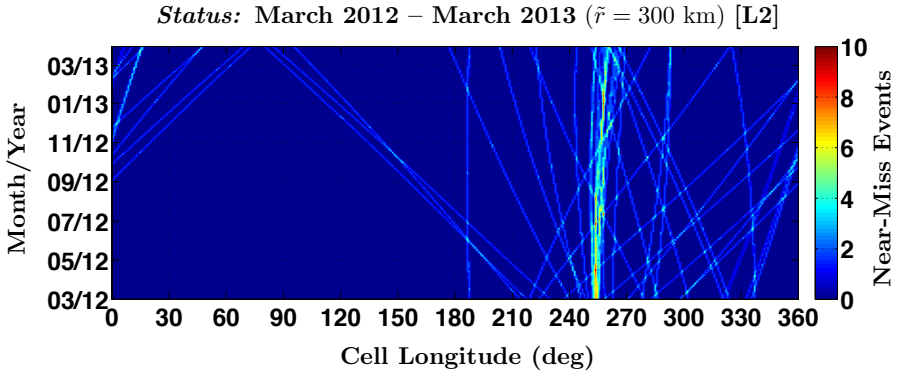

c) Western librating object (L2) contribution to near-miss CPE simulation.

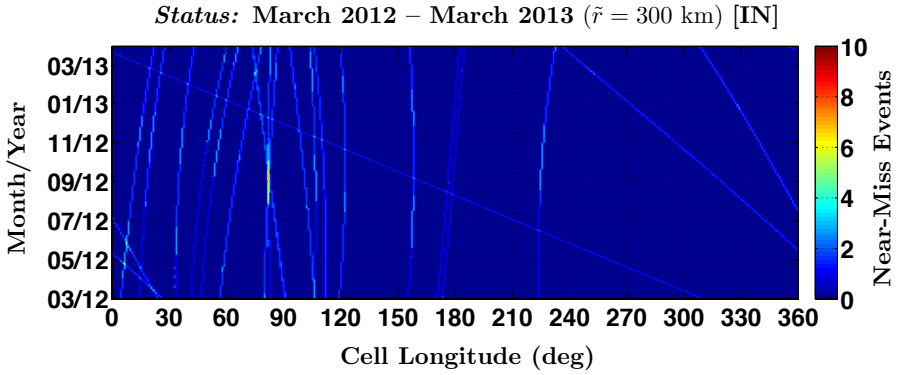

d) Indeterminate object (IN) contribution to near-miss CPE simulation.

Figure 8: Orbit class contributions to near-miss CPE for 300-km GEO torus.

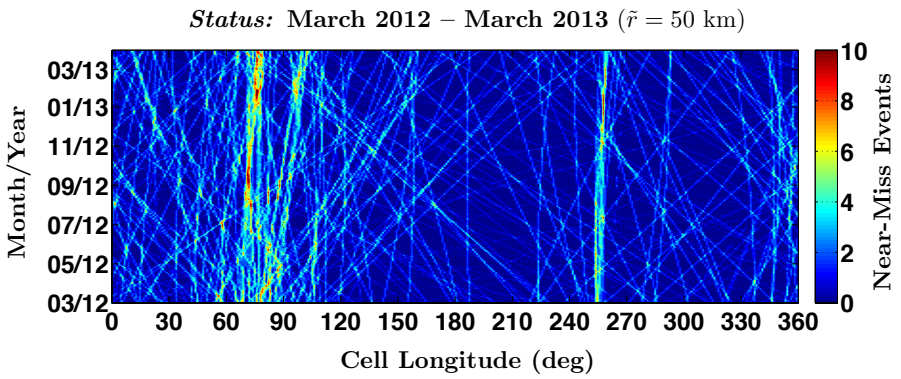

a) Near-miss CPE for March 2012 – March 2013 for 50-km GEO torus.

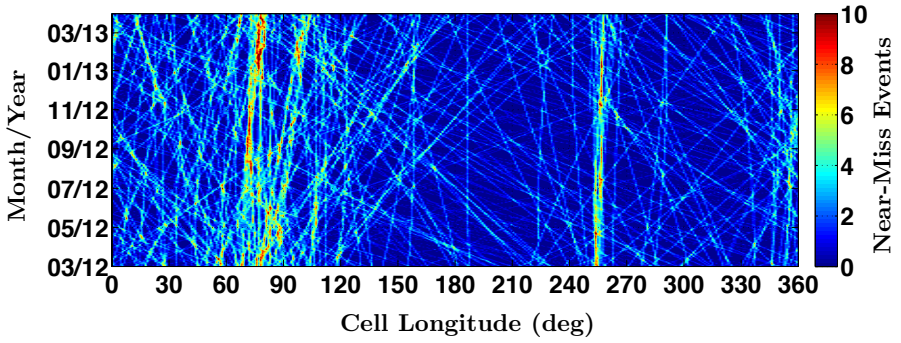

b) Near-miss CPE for March 2012 – March 2013 for 100-km GEO torus.

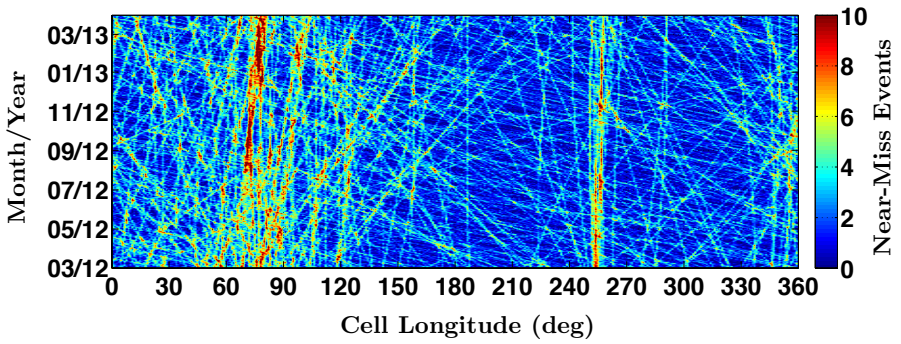

c) Near-miss CPE for March 2012 – March 2013 for 300-km GEO torus.

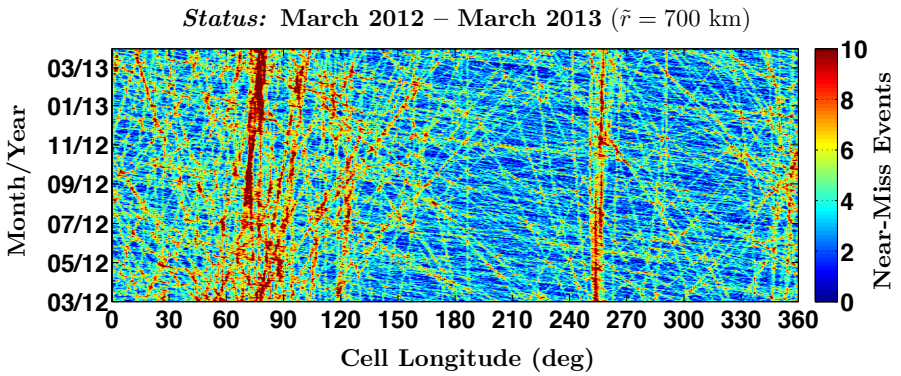

d) Near-miss CPE for March 2012 – March 2013 for 700-km GEO torus.

Figure 9: Near-miss CPE for March 2012 – March 2013 with nominal SRP.

References

[1] Jehn, R., Agapov, V., and Hernandez, C., "The Situation in the Geostationary Ring," *Advances in Space Research*, Vol. 35, 2005, pp. 1318–1327.

[2] Johnson, N., "Protecting the GEO Environment: Policies and Practices," *Space Policy*, Vol. 15, 1999, pp. 127–135.

[3] Wegener, P., Bendisch, J., Krag, H., Oswald, M., and Stabroth, S., "Population Evolution in the GEO Vicinity," *Advances in Space Research*, Vol. 34, 2004, pp. 1171–1176.

[4] Chrystal, P., McKnight, D., and Meredith, P., "Space Debris: On Collision Course for Insurers?" Tech. rep., Swiss Reinsurance Company Ltd, 2011.

[5] Yasaka, T., Hanada, T., and Hirayama, H., "GEO Debris Environment: A Model to Forecast the Next 100 Years," *Advances in Space Research*, Vol. 23, No. 1, 1999, pp. 191–199.

[6] Yasaka, T., *Space Debris: Hazard Evaluation and Mitigation*, ESI Book Series, Taylor and Francis, Inc., 2002, pp. 113–131.

[7] Klinkrad, H., *Space Debris: Models and Risk Analysis*, Praxis Publishing, 2006.

[8] Jehn, R. and Hernandez, C., "International Practices to Protect the Geostationary Ring," *Space Debris*, Vol. 1, 2001, pp. 221–233.

[9] Alfriend, K. T., Akella, M. R., Frisbee, J., Foster, J. L., Lee, D.-J., and Wilkins, M., "Probability of Collision Error Analysis," *Space Debris*, Vol. 1, May 1999, pp. 21–35.

[10] Klinkrad, H., Alarcon, J. R., and Sanchez, N., "Collision Avoidance for Operational ESA Satellites," *Proceedings of the Fourth European Conference on Space Debris*, August 2005.

[11] Liou, J.-C., Hall, D. T., Krisko, P. H., and Opiela, J. N., "LEGEND: A Three-Dimensional LEO-to-GEO Debris Evolutionary Model," *Advances in Space Research*, Vol. 34, 2004, pp. 981–986.

[12] Bendisch, J., Bunte, K., Klinkrad, H., Krag, H., Martin, C., Sdunnus, H., Walker, R., Wegener, P., and Wiedemann, C., "The MASTER-2001 Model," *Advances in Space Research*, Vol. 34, 2004, pp. 959–968.

[13] Lewis, H., Swinerd, G., Williams, N., and Gittins, G., "DAMAGE: A Dedicated GEO Debris Model Framework," *Proceedings of the Third European Conference on Space Debris*, Vol. 1, ESA Publications Division, March 2001.

[14] Liou, J.-C., "An Active Debris Removal Parametric Study for LEO Environmental Remediation," *Advances in Space Research*, Vol. 47, 2011, pp. 1865–1876.

[15] Flohrer, T., "Classification of Geosynchronous Objects: Issue 14," Tech. Rep. 1, European Space Operations Centre, February 2012.

[16] "Process for Limiting Orbital Debris," NASA-STD-8719.14 Change 4, National Aeronautics and Space Administration, September 2009.

[17] Flohrer, T., Choc, R., and Bastida, B., "Classification of Geosynchronous Objects: Issue 13," Tech. rep., European Space Operations Centre, February 2011.

[18] Schaub, H. and Junkins, J. L., *Analytical Mechanics of Space Systems*, American Institute of Aeronautics and Astronautics, Inc., 2nd ed., 2009.

[19] Curtis, H., *Orbital Mechanics for Engineering Students*, Elsevier Butterworth-Heinemann, 2005.

[20] Vallado, D., *Fundamentals of Astrodynamics and Applications*, Microcosm Press, 3rd ed., 2007.

[21] Schaub, H. and Jasper, L. E. Z., "Circular Orbit Radius Control using Electrostatic Actuation for 2-Craft Configurations," *Proceedings of the 2011 AAS/AIAA Astrodynamics Specialist Conference*, August 2011.

[22] Allan, R. R., "Perturbations of a Geostationary Satellite by the Longitude-Dependent Terms in the Earth's Gravitational Field," *Planetary and Space Science*, Vol. 11, August 1963, pp. 1325–1334.